

Simulation of crack propagation in alumina with ab-initio based polarizable force field

Stephen Hocker,¹ Philipp Beck,² Siegfried Schmauder,¹ Johannes Roth,² and Hans-Rainer Trebin²

¹*Institut für Materialprüfung, Werkstoffkunde und Festigkeitslehre (IMWF), Universität Stuttgart, Pfaffenwaldring 32, 70550 Stuttgart, Germany*

²*Institut für Theoretische und Angewandte Physik (ITAP), Universität Stuttgart, Pfaffenwaldring 57, 70550 Stuttgart, Germany*

(Dated: 8 November 2018)

We present an effective atomic interaction potential for crystalline α -Al₂O₃ generated by the program *potfit*. The Wolf direct, pairwise summation method with spherical truncation is used for electrostatic interactions. The polarizability of oxygen atoms is included by use of the Tangney-Scandolo interatomic force field approach. The potential is optimized to reproduce the forces, energies and stresses in relaxed and strained configurations as well as {0001}, {10 $\bar{1}$ 0} and {11 $\bar{2}$ 0} surfaces of Al₂O₃. Details of the force field generation are given, and its validation is demonstrated. We apply the developed potential to investigate crack propagation in α -Al₂O₃ single crystals.

I. INTRODUCTION

Aluminum oxide is the most commonly used ceramic in technological applications. Due to its insulating properties, it is frequently adopted in microelectronic devices, i.e., field effect transistors, integrated circuits or superconducting quantum interference devices. Another important field of application is the coating of metallic components. Alumina covering aluminum is known to prevent further oxidation of the metal. Since alumina is characterized by a high melting point and also a high degree of hardness, applications at high temperatures and high mechanical demands are possible. Mechanical properties such as tensile strengths and fracture processes are of high importance regarding these applications. Because surfaces and internal interfaces play an important part in these technologies, numerical modelling is often focused on such systems.

Due to this technological significance, alumina and metal/alumina interfaces were frequently investigated experimentally¹⁻³ and by *ab-initio* methods.⁴⁻⁷ First-principles methods are well established for calculating the work of separation or the surface energy. However, the investigation of dynamic processes such as crack propagation requires systems with significantly more atoms and larger timescales than *ab-initio* based methods nowadays can deal with. Hence, it is an important challenge to develop a suitable interaction force field for classical Molecular Dynamics (MD) simulations.

There exist interaction potential approaches for alumina, which reach a good accuracy by using angular dependent terms.^{8,9} Pair potentials are also widely applied in simulations of alumina¹⁰⁻¹³ by reason of usually much lower computational demands. Due to the lattice misfit, especially the simulation of interface structures has to be performed with many atoms. Hence, for the simulation of crack propagation, a pair potential is to be favored concerning the computational effort.

Many-body effects can be important for correctly describing bond angles and bond-bending vibration fre-

quencies in oxides. However, for SiO₂¹⁴⁻¹⁶ and MgO,¹⁶ it was shown that an accurate description can be achieved without angular dependent terms, but with polarizable oxygen atoms. There, the potential model of Tangney and Scandolo¹⁴ (TS) is applied, in which the dipole moments of oxygen atoms are determined self-consistently from the local electric field of surrounding charges and dipoles.

In Ref. 16, the computational effort in simulations scales linearly in the number of particles, which is due to the Wolf summation.¹⁷ We apply this combination of the TS model and the Wolf summation method in the potential generation as well as in simulations. An effective atomic interaction potential is generated with the program *potfit*.¹⁸ The potential parameters are optimized by matching the resulting forces, energies and stresses with respective *ab-initio* values with the force matching method.¹⁹ Simulations are performed with the MD code IMD.²⁰

A detailed description of the adopted methods and the potential generation is given in Sec. II. MD simulations and *ab-initio* calculations which were performed in order to validate the obtained force field are presented in Sec. III. As a first application of the new potential, we investigate crack propagation of alumina single crystals. To our knowledge, these are the first MD simulations of crack propagation in alumina with a potential that takes into account the polarizability of oxygen atoms. Results of these simulations are shown in IV. Finally, conclusions and an outlook are presented in Sec. V.

II. FORCE FIELD GENERATION

A. Tangney-Scandolo force field

The TS force field is a sum of two contributions: a short-range pair potential of Morse-Stretch (MS) form, and a long-range part, which describes the electrostatic interactions between charges and induced dipoles on the

oxygen atoms. The MS interaction between an atom of type i and an atom of type j has the form

$$U_{ij}^{\text{MS}} = D_{ij} \left[\exp[\gamma_{ij}(1 - \frac{r_{ij}}{r_{ij}^0})] - 2 \exp[\frac{\gamma_{ij}}{2}(1 - \frac{r_{ij}}{r_{ij}^0})] \right], \quad (1)$$

with $r_{ij} = |\mathbf{r}_{ij}|$, $\mathbf{r}_{ij} = \mathbf{r}_j - \mathbf{r}_i$ and the model parameters D_{ij} , γ_{ij} and r_{ij}^0 , which have to be determined during the force field generation.

Because the dipole moments depend on the local electric field of the surrounding charges and dipoles, a self-consistent iterative solution has to be found. In the TS approach, a dipole moment \mathbf{p}_i^n at position \mathbf{r}_i in iteration step n consists of an induced part due to an electric field $\mathbf{E}(\mathbf{r}_i)$ and a short-range part \mathbf{p}_i^{SR} due to the short-range interactions between charges q_i and q_j . Following Rowley *et al.*,²¹ this contribution is given by

$$\mathbf{p}_i^{\text{SR}} = \alpha_i \sum_{j \neq i} \frac{q_j \mathbf{r}_{ij}}{r_{ij}^3} f_{ij}(r_{ij}) \quad (2)$$

with

$$f_{ij}(r_{ij}) = c_{ij} \sum_{k=0}^4 \frac{(b_{ij} r_{ij})^k}{k!} e^{-b_{ij} r_{ij}}. \quad (3)$$

b_{ij} and c_{ij} are parameters of the model. Together with the induced part, one obtains

$$\mathbf{p}_i^n = \alpha_i \mathbf{E}(\mathbf{r}_i; \{\mathbf{p}_j^{n-1}\}_{j=1,N}, \{\mathbf{r}_j\}_{j=1,N}) + \mathbf{p}_i^{\text{SR}}, \quad (4)$$

where α_i is the polarizability of atom i and $\mathbf{E}(\mathbf{r}_i)$ the electric field at position \mathbf{r}_i , which is determined by the dipole moments \mathbf{p}_j in the previous iteration step. Taking into account the interactions between charges U^{qq} , between dipole moments U^{pp} and between a charge and a dipole U^{pq} , the total electrostatic contribution is given by

$$U^{\text{EL}} = U^{\text{qq}} + U^{\text{pq}} + U^{\text{pp}}, \quad (5)$$

and the total interaction is

$$U^{\text{tot}} = U^{\text{MS}} + U^{\text{EL}}. \quad (6)$$

B. Wolf summation

The electrostatic energies of a condensed system are described by functions with r^{-n} dependence, $n \in \{1, 2, 3\}$. For point charges (r^{-1}) it is common to apply the Ewald method, where the total Coulomb energy of a set of N ions,

$$E^{\text{qq}} = \frac{1}{2} \sum_{i=1}^N \sum_{\substack{j=1 \\ j \neq i}}^N \frac{q_i q_j}{r_{ij}}, \quad (7)$$

is decomposed into two terms E_r^{qq} and E_k^{qq} by inserting a unity of the form $1 = \text{erfc}(\kappa r) + \text{erf}(\kappa r)$ with the error function

$$\text{erf}(\kappa r) := \frac{2}{\sqrt{\pi}} \int_0^{\kappa r} dt e^{-t^2}. \quad (8)$$

The splitting parameter κ controls the distribution of energy between the two terms. The short-ranged erfc term is summed up directly, while the smooth erf term is Fourier transformed and evaluated in reciprocal space. This restricts the technique to periodic systems. However, the main disadvantage is the scaling of the computational effort with the number of particles in the simulation box, which increases as $O(N^{3/2})$,²² even for the optimal choice of κ .

Wolf *et al.*¹⁷ designed a method with linear scaling properties $O(N)$ for Coulomb interactions. By taking into account the physical properties of the system, the reciprocal-space term E_k^{qq} is disregarded. It can be written as

$$E_k^{\text{qq}} = \frac{2\pi}{V} \sum_{\substack{\mathbf{k} \neq \mathbf{0} \\ |\mathbf{k}| < k_c}} S(\mathbf{k}) \frac{\exp(-\frac{|\mathbf{k}|^2}{4\kappa^2})}{|\mathbf{k}|^2}, \quad (9)$$

where $S(\mathbf{k})$ is the charge structure factor and V the volume of the simulation box. The charge structure factor is the Fourier transform of the charge-charge autocorrelation function. In condensed matter, the charges screen each other; the approach yields proper results in liquids and largely also in solids. This means that for small magnitudes of the wave vectors \mathbf{k} , the charge structure factor is also small. In previous studies^{16,23} it was shown that the reciprocal-space term is indeed negligible compared to the real-space part, provided that the splitting parameter κ is chosen small enough. As however a smaller κ results in a larger real-space cutoff r_c , the latter has to be chosen three or four times the size of a typical short-range cutoff radius in metals. In a recent study¹⁶ a cutoff radius of only 8 Å was sufficient to describe the electrostatics of liquid silica and magnesia accurately.

In addition, a continuous and smooth cutoff of the remaining screened Coulomb potential $\tilde{E}^{\text{qq}}(r_{ij}) = q_i q_j \text{erfc}(\kappa r_{ij}) r_{ij}^{-1}$ is adopted at r_c by shifting the potential so that it goes to zero smoothly in the first two derivatives at $r = r_c$. We use the Wolf method for Coulomb and dipolar interactions. For more information about the Wolf summation of dipole contributions, the estimation of errors attended by this method and a detailed analysis of the energy conservation in MD simulations see Ref. 23.

C. Generation with potfit

The programm *potfit* generates an effective atomic interaction force field solely from *ab-initio* reference struc-

tures. The potential parameters are optimized by matching the resulting forces, energies and stresses to according first-principles values with the force matching method. All reference structures used in this study were prepared with the first-principles plane wave code VASP.^{24,25} For N_m particles, reference configuration m provides one energy e_m^0 , six components of the stress tensor $s_{m,l}^0$ ($l = 1, 2, \dots, 6$) and $3N_m$ total force cartesian components $f_{m,n}^0$ ($n = 1, 2, \dots, 3N_m$) on N_m atoms. The function

$$Z = w_e Z_e + w_s Z_s + Z_f \quad (10)$$

is minimized, where

$$\begin{aligned} Z_e &= 3 \sum_{m=1}^M N_m (e_m - e_m^0)^2, \\ Z_s &= \frac{1}{2} \sum_{m=1}^M \sum_{l=1}^6 N_m (s_{m,l} - s_{m,l}^0)^2, \\ Z_f &= \sum_{m=1}^M \sum_{n=1}^{3N_m} (f_{m,n} - f_{m,n}^0)^2, \end{aligned} \quad (11)$$

and e_m , $s_{m,l}$ and $f_{m,n}$ are the corresponding values calculated with the parametrized force field. w_e and w_s are weights to balance the different amount of available data for each quantity. They are defined in such a way, that each weight can be taken as the percentual amount of the concerning force data. In the following we assume M reference structures that all consist of the same number of particles ($N_m = N$), but in principle, *potfit* can handle any different number of particles for each reference structure. The root mean square (rms) errors,

$$\Delta F_e = \sqrt{\frac{Z_e}{3MN}}, \quad \Delta F_s = \sqrt{\frac{2Z_s}{MN}} \quad \text{and} \quad \Delta F_f = \sqrt{\frac{Z_f}{MN}}, \quad (12)$$

are first indicators of the quality of the generated force field. Their magnitudes are independent of weighting factors, number and sizes of reference structures. For the minimization of the force field parameters, a combination of a stochastic simulated annealing algorithm²⁶ and a conjugate-gradient-like deterministic algorithm²⁷ is used. For more information about the implementation of long-range electrostatic interactions including the TS force field with Wolf summation see Ref. 16.

D. Parametrization

We first prepared a set of 67 α -alumina crystal structures with 360 atoms, in total 24 120 atoms. This reference database is composed of three kinds of structures: (i) crystals strained up to 20% in $[0001]$, $[\bar{2}110]$ and $[0\bar{1}10]$ directions at zero Kelvin, (ii) structures with free (0001), $(\bar{2}110)$ and $(0\bar{1}10)$ surfaces at zero Kelvin and (iii) equilibrated snapshots taken out of an *ab-initio* MD trajectory, where an ideal crystal is heated from zero Kelvin up to

q_{Al}	q_{O}	α_{O}	$b_{\text{Al-O}}$	$c_{\text{Al-O}}$
1.122 608	-0.748 406	0.026 576	18.984 286	-5.571 329
		D	γ	r^0
Al-Al		0.000 890	12.737 442	5.405 175
Al-O		1.000 058	8.077 778	1.851 806
O-O		0.005 307	12.081 851	3.994 815

TABLE I. Force field parameters, given in IMD units set eV, Å and amu (hence charges are multiples of the elementary charge).

2000 Kelvin. It has to be mentioned that no initial ad-hoc potential as used in Refs. 14 and 16 is required to generate a reference database. This is only necessary in the case of liquid structures. The present work, however, deals with crystalline structures where a database can be generated without need of classical MD trajectories. The 67 structures are applied as input configurations for the first-principles plane wave code VASP.^{24,25} We used ultrasoft pseudopotentials²⁸ and the Perdew-Wang 91²⁹ generalized gradient approximation (GGA) to the exchange-correlation functional. The latter is recommended in Ref. 16. A plane wave cutoff of 396 eV was used. We adopt a gamma centered k mesh of $2 \times 2 \times 2$ k points. The weights in *potfit* were chosen to $w_e = 0.03$ and $w_s = 0.28$. Setting $\kappa = 0.1 \text{ \AA}^{-1}$, a cutoff radius of 10 Å was found to be sufficient. The final set of parameters is shown in Table I. The rms errors are $\Delta F_e = 0.0492$ eV, $\Delta F_s = 0.0273 \text{ eV \AA}^{-3}$ and $\Delta F_f = 0.3507 \text{ eV \AA}^{-1}$.

III. VALIDATION

Firstly, we determine basic properties of crystalline alumina such as lattice constants, cohesive energies and vibrational properties. Additionally and relevant for fracture studies, our validation simulations focus on surface relaxations, surface energies and stresses of strained configurations. Finally, we probe the new potential beyond its optimization range by investigating two basal twins.

Lattice constants and cohesive energies are obtained by pressure relaxation: Besides energy minimization, the pressure tensor of the sample is calculated at each step, and the size of the simulation box is changed by a small amount in order to lower that pressure. After inserting surfaces or interfaces into the relaxed sample, a further relaxation is performed which reveals surface or interface energies. The *ab-initio* calculations of these properties are performed with VASP, as described in section II D. As can be seen from Table II, the lattice constants and the cohesive energy of crystalline α -alumina obtained with the new potential agree well with our *ab-initio* calculations and previous studies.

The *partial* vibrational density of states (VDOS) for $G_{\text{Al}}(\text{E})$ and $G_{\text{O}}(\text{E})$ was obtained by computing the Fourier transform of the time-dependent velocity-velocity autocorrelation function from a 100 ps MD trajectory

	a (Å)	c (Å)	E_{coh} (eV)	$E_{\{0001\}}$ (J/m ²)	$E_{\{11\bar{2}0\}}$ (J/m ²)	$E_{\{10\bar{1}0\}}$ (J/m ²)	$E_{\text{twin}}^{\text{m}}$ (J/m ²)	$E_{\text{twin}}^{\text{r}}$ (J/m ²)
New potential	4.79	12.97	31.85	1.59	1.65	1.89	1.32	0.57
Ab-initio	4.78	13.05	32.31	1.55	1.83	1.98	2.12	0.76
Lit. (experiment)	4.76 ³⁰	13.00 ³⁰	31.8 ³¹					
Lit. (ab-initio)			33.0 ³²	1.85 ³³ 2.03 ³⁴ 1.76 ³⁵ 1.54 ³⁶	2.44 ³³ 2.23 ³⁴	2.39 ³³ 2.50 ³⁴	1.99 ⁴	0.73 ⁴

TABLE II. Lattice constants, cohesive energies and interface energies of basal twins obtained with the new potential compared to *ab-initio* results and literature data.

with the software package nMoldyn.³⁷ The *generalized* VDOS $G(E)$ is then calculated by

$$G(E) = \sum_{\mu=\text{Al,O}} \frac{\sigma_{\mu}}{m_{\mu}} G_{\mu}(E) \quad (13)$$

with the scattering cross section σ_{μ} and atomic mass m_{μ} of atom μ . Fig. 1 shows the partial and generalized VDOS. The key features of the curves obtained with the new potential and an *ab-initio* study from Ref. 38 coincide. For the partial VDOS of aluminum, both studies show a broad band between 41 and 83 meV. The *ab-initio* results show less states in the low-energy band between 15 and 30 meV. There are two sharp peaks between 87 and 100 meV in the *ab-initio* curve, whereas the new potential shows one broader peak with a shoulder, that indicated the second peak. The curves for the partial VDOS of oxygen are in good agreement. Both simulation and *ab-initio* calculation show the main band of states between 12 and 85 meV with similar curve progression and three local maxima at around 35, 47 and 62 meV. These characteristics are also reflected in the generalized VDOS. In addition, the generalized VDOS obtained with neutron scattering¹ is depicted, which shows the same main characteristics of the curve on a qualitative level.

The literature surface energies^{33–36} given in Table II differ among each other which origins from the different methods used in the *ab-initio* approaches. Our calculation of the (0001) surface energy agrees with the value obtained in Ref. 36, where also the VASP code with the same pseudopotential and exchange-correlation approximation was used. For all investigated surfaces, the energies obtained with the new potential and with *ab-initio* methods agree. Both results reveal that the (0001) surface has the lowest surface energy and the (0 $\bar{1}$ 10) surface the highest one. The studies of Ref. 33–35 yield slightly higher energies for all investigated surfaces.

The surface structure after relaxation is shown in Fig. 2. It reveals that the Al atoms of the outermost Al-layer are moved closer to the outermost O-layer at the (0001) Al-terminated surface, which is known to be the most stable (0001) surface termination. The atomic adjustment perpendicular to the surface obtained with the new potential agrees very well with our *ab-initio* results. The distance of an Al- and an O-layer is 0.83 Å,

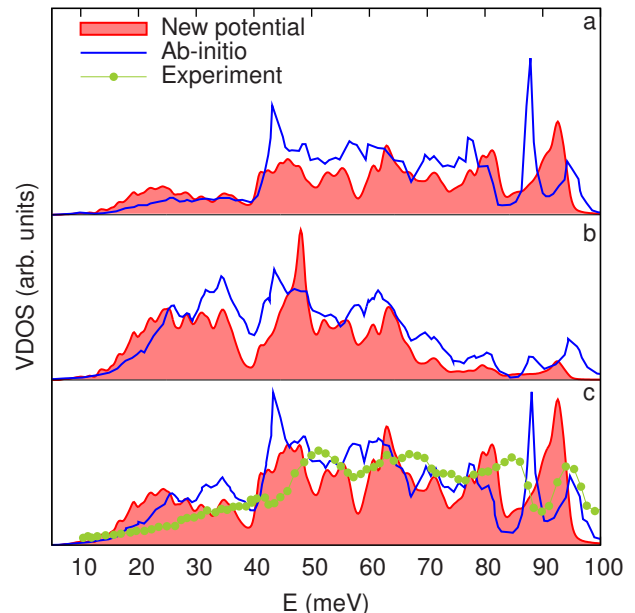


FIG. 1. VDOS calculated with the new potential compared with an *ab-initio* study³⁸ and experiment.¹ a) Partial VDOS for aluminum atoms, b) partial VDOS for oxygen atoms, c) generalized VDOS.

whereas this value decreases to 0.15 Å (MD) respectively 0.14 Å (*ab-initio*) at the surface. A relaxation of the oxygen atoms can be seen at the (0 $\bar{1}$ 10) surface. Both MD and *ab-initio* study show that the three oxygen atoms per unit cell – which are initially in a row along the direction orthogonal to the plane of Fig. 2 – relax to different distances from the initial surface. Furthermore, a relaxation towards the neighboring Al-atoms in the first layer occurs. The results obtained with the new potential again coincide with the *ab-initio* calculation. One difference, however, can be seen at the second layer: Every second Al atom in each row orthogonal to the figure plane is slightly displaced towards the surface in the *ab-initio* relaxation. This effect is not observed in the MD relaxation simulation. Neither the MD nor the *ab-initio* relaxation study of the ($\bar{2}$ 110) surface yield significant atomic movements.

As described in section IID, strained configurations

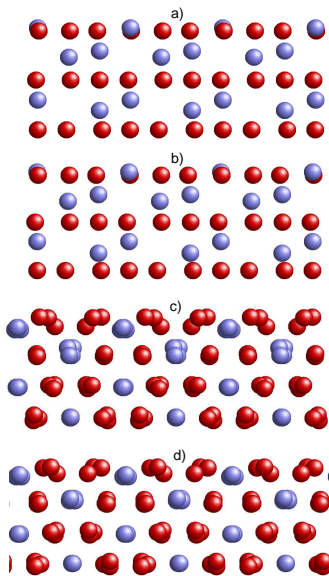


FIG. 2. Surface relaxations for the new potential compared with *ab-initio* calculations. Red: oxygen. Blue: aluminum. a) (0001)-surface, *ab-initio*, b) (0001)-surface, MD, c) (0 $\bar{1}$ 10)-surface, *ab-initio*, d) (0 $\bar{1}$ 10)-surface, MD.

with strain directions [0001], [$\bar{2}$ 110] and [0 $\bar{1}$ 10] were added in the reference database for the potential optimization approach. To clarify, whether the new potential can reproduce the stresses of strained configurations, these stresses are calculated using MD with the new potential.

Fig. 3 shows a comparison of stresses obtained in simulations to the stresses of the underlying *ab-initio* reference configurations, each with 360 atoms. They are strained up to 15% in [0001], [$\bar{2}$ 110] and [0 $\bar{1}$ 10] direction respectively. The difference between MD and *ab-initio* results is small at lower strains. With increasing strain, the difference increases up to about 10 GPa at 15% strain. The new potential underestimates the stress in all cases. However, the directions, in which the stress increases, can be reproduced correctly: The highest stresses are observed for strains in [0001] direction, the lowest stresses are found for configurations strained in [0 $\bar{1}$ 10] direction.

Finally, we probe the potential by simulating basal twins. These are systems which were not included in the optimization process. This demonstrates the applicability of the new force field beyond the range for which it was optimized. It is well known that the basal twin is a frequently observed Al_2O_3 interface.³⁹ We consider two types of basal twins which differ by their interface structure: The mirror twin consists of two single crystal elementary cells with mirror symmetry. The mirror plane is a (0001) oriented oxygen layer. Based on the mirror twin, one can obtain the rotation twin by shifting one of the single crystal elementary cells in the [0 $\bar{1}$ 10] direction. For details of the interface structures see Ref. 4. As can be seen from Table II, the *ab-initio* calculated interface energies of the basal twins agree well with the

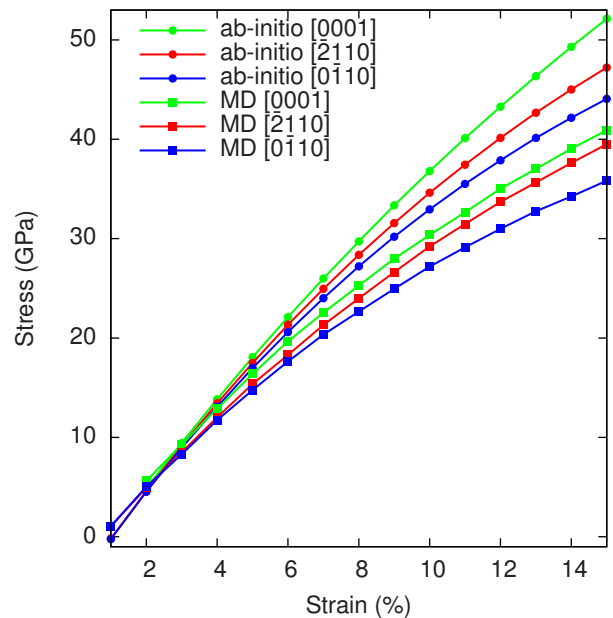


FIG. 3. Stresses of strained configurations with [0001] (green), [$\bar{2}$ 110] (red) and [0 $\bar{1}$ 10] (blue) strain directions against the stress tensor component in direction of strain. The curves obtained with the new potential are marked with squares, those from *ab-initio* calculations with circles.

results from Ref. 4. The MD simulations with the new potential underestimate both energy values. But the potential is able to qualitatively reproduce the relation of the two interface energies: The interface energy of the mirror twin ($E_{\text{twin}}^{\text{m}}$) is about two by three times the one of the rotation twin ($E_{\text{twin}}^{\text{r}}$); that is why, the latter one is energetically favorable.

IV. CRACK PROPAGATION

A. Simulation conditions

To investigate crack propagation in mode I at constant energy release rate, we prepared configurations with dimensions (b_x, b_y, b_z) of $21 \times 3 \times 13 \text{ nm}^3$ which contain about 80 000 atoms. Lateral planes of these cuboids are the (0001), (0 $\bar{1}$ 10) and ($\bar{2}$ 110) crystallographic planes. An elliptical initial crack of 5 nm length in x-direction is inserted on one side of the samples by moving atoms in z-direction. The opening of the crack is calculated with the Griffith criterion: In front of the crack tip the sample is linearly strained until the elastic energy due to strain is equal to the Griffith energy G_0 which is twice the surface energy of the crack plane. This criterion was fulfilled at about 4% strain. These structures are then relaxed to obtain the displacement field of a stable crack. Periodic boundary conditions are applied in the direction along the crack front, whereas fixed displacement boundary conditions are applied in the other directions.

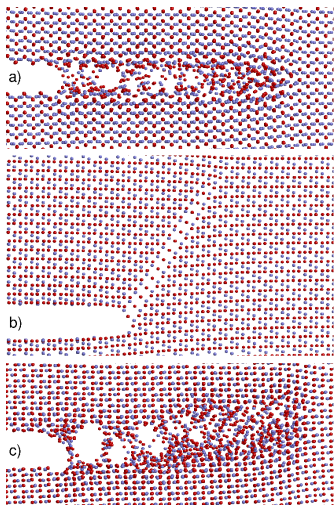


FIG. 4. Crack propagation in α - Al_2O_3 (Al-atoms blue, O-atoms red). a) Initial crack in $(\bar{2}110)$ plane, b) initial crack in (0001) plane, c) initial crack in $(0\bar{1}10)$ plane.

Initial configurations for crack propagation simulations with different energy release rates are obtained by a linear scaling of this displacement field. During the crack propagation simulations, the NVE (constant number of particles, volume and energy) ensemble and a starting temperature of 0 K are applied. A timestep of 1 fs is used for all simulations.

B. Cracks in a $\{11\bar{2}0\}$ plane

Initial cracks were inserted in a $(\bar{2}110)$ plane with crack propagation directions $[0001]$ or $[0\bar{1}10]$. In both cases, the initial crack is stationary at energy release rates up to $1.5 G_0$. Higher energy release rates lead to crack propagation in the initial $(\bar{2}110)$ plane. It is known that the discrete character of interatomic bonds which reveals itself in the so called lattice trapping effect⁴⁰ can retard crack propagation to energy release rates beyond the critical energy release rate determined by the Griffith criterion. As can be seen from Fig. 4 a, yet at high energy release rates bond breaking between the two crack lips is not continuous. Chains of atoms bridging the crack lips stay intact during the simulation. Furthermore, considerable disorder is observed at the resulting crack surfaces. In $[0\bar{1}10]$ propagation direction, these effects are slightly more pronounced than in $[0001]$ propagation direction. It cannot be ruled out that these very strong bonds are caused by inaccuracies of the force field. However, the observation of intact bonds bridging the crack lips agree with previous simulations of alumina, where it was stated that these atomic chains were observed in experiments as well.¹³ Our results show that cracks are able to propagate in $(\bar{2}110)$ planes in both $[0001]$ and $[0\bar{1}10]$ directions. This is in accordance with experiments,² where it turned out that cracks occur in $\{11\bar{2}0\}$ planes although these are

not the preferred fracture planes.

C. Cracks in a $\{0001\}$ plane

The $\{0001\}$ planes are the closest packed planes of α - Al_2O_3 ; therefore cleavage of these planes is improbable. Our simulations confirm that cracks do not propagate in the (0001) plane in which the initial crack was inserted with crack propagation directions $[\bar{2}110]$ or $[0\bar{1}10]$. At energy release rates below $1.7 G_0$, a damaged region in front of the crack tip is generated with atomic disorder similar to the case of the $(\bar{2}110)$ plane. However, the crack tip does not move. More interesting is the $(0001)[0\bar{1}10]$ oriented initial crack at higher energy release rates: As can be seen from Fig. 4 b, the crack propagates in a $\{10\bar{1}2\}$ cleavage plane. Due to the boundary conditions, the crack surfaces cannot separate completely, but a row of oxygen atoms stays in the crack path. In contrast to the cracks in a $\{11\bar{2}0\}$ plane, there is no disorder along the crack surfaces. The observed crack propagation in a $\{10\bar{1}2\}$ cleavage plane agrees well with electron microscopy investigations² which revealed that fracture surfaces of the $\{1012\}$ cleavage planes are frequently observed in alumina.

D. Cracks in a $\{10\bar{1}0\}$ plane

Cracks initially inserted in a $(0\bar{1}10)$ plane in $[\bar{2}110]$ direction propagate in this orientation starting at energy release rates of $2.2 G_0$. In the case of a $[0001]$ crack propagation direction (Fig. 4 c), the movement of the crack tip was observed at energy release rates above $1.9 G_0$. Similar to the case of the $(0001)[0\bar{1}10]$ orientation, the crack changes its propagation plane. As can be seen in Fig. 4 c, the crack moves partially in the initial $(0\bar{1}10)$ plane, but also partially in a $\{10\bar{1}2\}$ cleavage plane. As in the case of cracks in $\{11\bar{2}0\}$ planes, the initially $(0\bar{1}10)[\bar{2}110]$ or $(0\bar{1}10)[0001]$ oriented cracks generate disorder at the crack surfaces during crack propagation; some atomic bonds stay intact across the crack opening.

E. Orientation of electric dipole moments

The orientation of electric dipole moments in crack propagation simulations can differ significantly from the orientations in other configurations of the same material. There are two main effects which influence the alignment of dipoles: Charged surfaces and piezoelectricity. In order to investigate these effects in α - Al_2O_3 , dipoles of the crack propagation simulations are visualized with the program MegaMol.⁴¹ Since effects from the boundary conditions (which involve unnatural surfaces in some directions) should be excluded, we performed a crack propagation simulation with periodic boundary conditions in

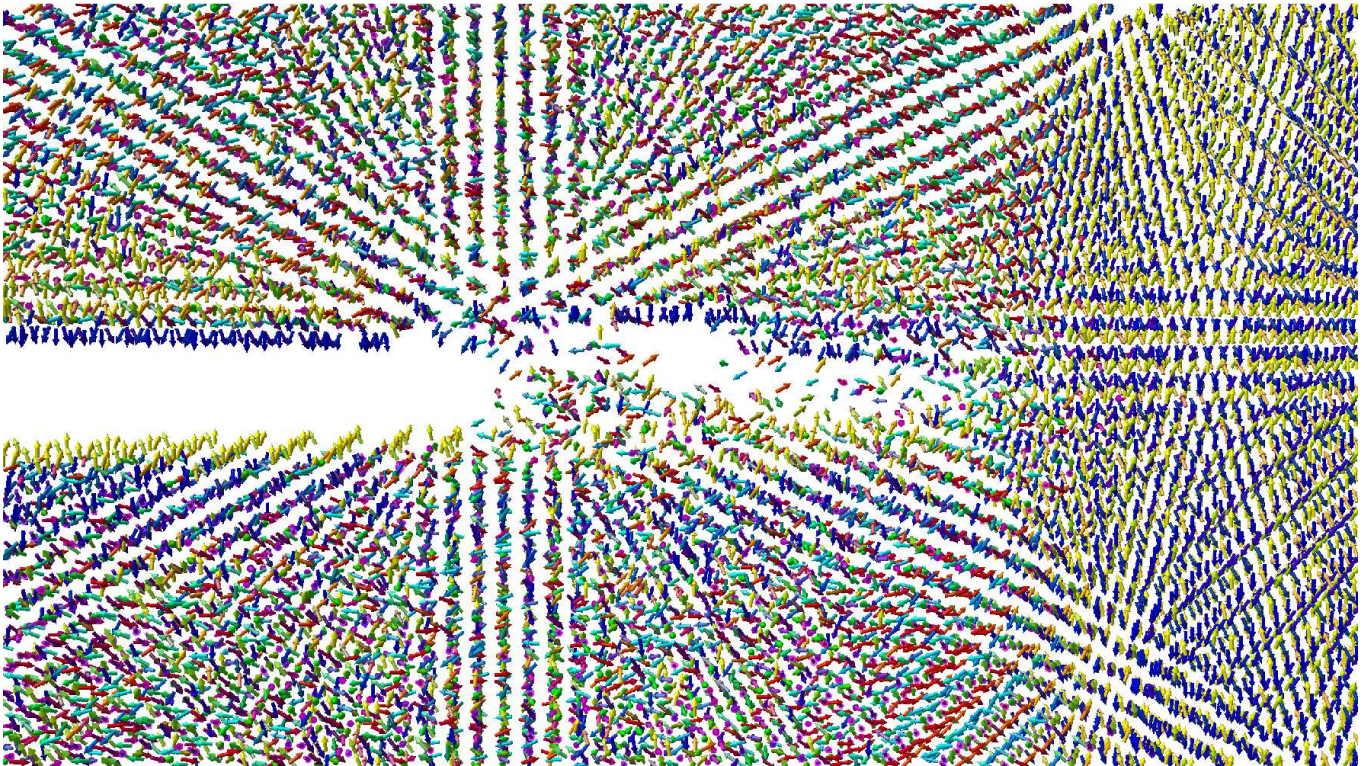


FIG. 5. Electric dipole moments of oxygen atoms in crack propagation simulation. Each oxygen atom is visualized by an arrow with the direction of the dipole moment; the lengths are normalized. The colour corresponds to the orientation: blue – down, yellow – up, green – left, red – right.

all directions. In this case, a symmetrical crack was inserted in the middle of the sample. As long as the two crack tips are far away from each other (which is true up to about 5 nm distance), we observe the same result as with the boundary conditions described above. Hence, possible boundary condition effects can be excluded.

Charged crack surfaces occur as a function of the crack propagation planes. As shown in Fig. 4, the initial surfaces of cracks in a $\{11\bar{2}0\}$ plane are oxygen terminated. Therefore, it can be expected that the dipoles of the oxygen atoms at each crack surface are aligned in the same direction and the alignment on the other crack surface is the other way round. This adjustment is reproduced in our simulation, as can be seen in Fig. 5. It is significantly more pronounced at the surfaces of the initial crack (left part of the crack in Fig. 5), but it can be seen also along the crack surfaces created by the propagation (right part of the crack). In the latter case, the disorder along the crack surfaces and the intact atomic chains across the crack opening reduce the alignment.

Collective orientation mechanisms of electric dipole moments due to strain can only be observed in crystals, where the inversion symmetry is broken. Therefore, in bulk α - Al_2O_3 usually no dipole alignment is observed. With the new force field, we simulated α - Al_2O_3 strained in $[\bar{2}110]$ direction up to 15%. No collective alignment of dipole moments occurred in this simulation. In the crack

propagation simulation, however, the inversion symmetry is broken by the crack. As can be seen from Fig. 5, an orientation of the electric dipole moments due to strain is observed. Dipoles are aligned in the region in front of the crack tip which corresponds to the strained part of the configuration. On the contrary, in the unstrained regions below and above the crack surfaces the dipoles show no preferred orientation.

V. CONCLUSIONS

We presented the generation and validation of an effective *ab-initio* based polarizable force field for MD simulations of α - Al_2O_3 . It was shown that it can be used to simulate mechanical and vibrational properties of crystalline alumina with high accuracy. Furthermore, the potential is designed for the simulation of surfaces, notably for crack propagation. Due to the Wolf summation, we achieve linear scaling properties in the number of particles, which makes it possible to investigate typical required system sizes and time scales for crack simulations in reasonable real time. The polarizability of oxygen atoms is taken into account by use of the Tangney-Scandolo interatomic force field approach. To our knowledge, the present work is the first study of the behavior of electric dipole moments in MD simulations on

crack propagation.

As a first application beyond the study of basic crystalline properties, we performed crack propagation simulations with initial cracks in different crystallographic planes of α -Al₂O₃. We have shown that cracks usually propagate in the initial plane, but no crack propagation occurs in the close packed {0001} planes. It was also observed that cracks tend to deflect to a {10 $\bar{1}$ 2} cleavage plane in the case of an initial crack plane which is unfavourable regarding crack propagation. The simulation result, that {10 $\bar{1}$ 2} cleavage planes are favourable regarding crack propagation, agrees well with electron microscopy investigations² of cracks in α -Al₂O₃. Additionally, it was shown that the new force field allows to investigate electric dipole orientations in various strained structures. Dipole alignment due to strain in α -Al₂O₃ was found in the performed crack propagation simulations.

In the future, the new force field can be applied for large scale simulations of alumina systems, particularly with regard to surfaces and interfaces, e.g. polycrystals, or multi-layer composites. The new force field allows further increasing of system sizes to several millions of atoms at time scales up to 1 ns.

ACKNOWLEDGMENTS

Support from the DFG through Collaborative Research Centre 716, Project B.1 and B.2 is gratefully acknowledged. The authors thank Holger Euchner for helpful discussions concerning vibrational properties of condensed materials, and Sebastian Grottel for the collaboration regarding the visualization with MegaMol.

¹C.-K. Loong, J. Eur. Cer. Soc. **19**, 2241 (1999).

²H. Matsuo, M. Mitsuhara, K. Ikeda, S. Hata, and H. Nakashima, Int. J. Fatigue **32**, 592 (2010).

³A. G. Evans, M. C. Lu, S. Schmauder, and M. Rühle, Acta Metall. **34**, 1643 (1986).

⁴A. G. Marinopoulos, S. Nufer, and C. Elsässer, Phys. Rev. B **63**, 165112 (2001).

⁵W. Zhang and J. R. Smith, Phys. Rev. Lett. **85**, 3225 (2000).

⁶W. Zhang and J. R. Smith, Phys. Rev. B **61**, 16883 (2000).

⁷S. V. Eremeev, S. Schmauder, S. Hocker, and S. E. Kulkova, Physica B **404**, 2065 (2009).

⁸P. Vashishta, R. K. Kalia, A. Nakano, and J. P. Rino, J. Appl. Phys. **103**, 083504 (2008).

⁹S. Blonski and S. H. Garofalini, Surf. Sci. **295**, 263 (1993).

¹⁰C. T. Bodur, J. Chang, and A. S. Argon, J. Eur. Cer. Soc. **25**, 1431 (2005).

¹¹V. Van Hoang, Phys. Rev. B **70**, 134204 (2004).

¹²J. Sun, T. Stirner, and A. Matthews, Surf. Sci. **601**, 1358 (2007).

¹³W. Wunderlich and H. Awaji, Material & Design **22**, 53 (2001).

¹⁴P. Tangney and S. Scandolo, J. Chem. Phys. **117**, 8898 (2002).

¹⁵J. R. Kermode, S. Cereda, P. Tangney, and A. De Vita, J. Chem. Phys. **133**, 094102 (2010).

¹⁶P. Beck, P. Brommer, J. Roth, and H.-R. Trebin, J. Chem. Phys. **135**, 234512 (2011).

¹⁷D. Wolf, P. Koblinski, S. R. Phillpot, and J. Eggebrecht, J. Chem. Phys. **110**, 8254 (1999).

¹⁸P. Brommer and F. Gähler, Modelling Simul. Mater. Sci. Eng. **15**, 295 (2007), <http://www.itap.physik.uni-stuttgart.de/~imd/potfit/>.

¹⁹F. Ercolessi and J. B. Adams, Europhys. Lett. **26**, 583 (1994).

²⁰J. Stadler, R. Mikulla, and H.-R. Trebin, Int. J. Mod. Phys. C **8**, 1131 (1997), <http://www.itap.physik.uni-stuttgart.de/~imd/>.

²¹A. J. Rowley, P. Jemmer, M. Wilson, and P. A. Madden, J. Chem. Phys. **108**, 10209 (1998).

²²D. Fincham, Mol. Sim. **13**, 1 (1994).

²³P. Brommer, P. Beck, A. Chatzopoulos, F. Gähler, J. Roth, and H.-R. Trebin, J. Chem. Phys. **132**, 194109 (2010).

²⁴G. Kresse and J. Hafner, Phys. Rev. B **47**, 558 (1993).

²⁵G. Kresse and J. Furthmüller, Phys. Rev. B **54**, 11169 (1996).

²⁶A. Corona, M. Marchesi, C. Martini, and S. Ridella, ACM Trans. Math. Softw. **13**, 262 (1987).

²⁷M. J. D. Powell, Comp. J. **7**, 303 (1965).

²⁸G. Kresse and D. Joubert, Phys. Rev. B **59**, 1758 (1999).

²⁹J. P. Perdew, J. A. Chevary, S. H. Vosko, K. A. Jackson, M. R. Pederson, D. J. Singh, and C. Fiolhais, Phys. Rev. B **46**, 6671 (1992).

³⁰P. Villars and L. D. Calvert, *Pearson's Handbook of Crystallographic Data for Intermetallic Phases, 2nd Edition, Vol. I* (ASM International, Materials Park, Ohio, 1991) p. 970.

³¹R. C. Weast, ed., *CRC Handbook of Chemistry and Physics* (CRC Press, Boca Raton, FL, 1983).

³²D. J. Siegel, L. G. Hector Jr., and J. B. Adams, Phys. Rev. B **67**, 092105 (2003).

³³J. Sun, T. Stirner, and A. Matthews, Surf. Coat. Tech. **201**, 4205 (2006).

³⁴W. C. Mackrodt, R. J. Davey, S. N. Black, and R. Docherty, J. Cryst. Growth **80**, 441 (1987).

³⁵I. Manassidis, A. De Vita, and M. J. Gillan, Surf. Sci. Lett. **285**, L517 (1993).

³⁶H. P. Pinto, R. M. Nieminen, and S. D. Elliot, Phys. Rev. B **70**, 125402 (2004).

³⁷T. Rog, K. Murzyn, K. Hinsen, and G. R. Kneller, J. Comput. Chem. **24**, 657 (2003).

³⁸Z. Lodziana and K. Parlinski, Phys. Rev. B **67**, 174106 (2003).

³⁹K. J. Morrissey and C. B. Carter, J. Am. Ceram. Soc. **67**, 292 (1984).

⁴⁰R. Thomson, C. Hsieh, and V. Rana, J. Appl. Phys. **42**, 3154 (1970).

⁴¹MegaMol, <http://www.visus.uni-stuttgart.de/megamol/>.